International Journal of Computational and Experimental Science and ENgineering (IJCESEN)

Vol. 12-No.3 (2026) pp. 123-138
http://www.ijcesen.com

ISSN: 2149-9144

Research Article

Enhancing Grid Stability Using a Fuzzy Logic Controlled 800 kW PV-STATCOM System

Leila Boukarana[1] *, Yassina Medghaghet [2]

[1]Faculty of Hydrocarbons and Chemistry, University of M'Hamed Bougara – Boumerdes, 35000, Alegria.
* **Corresponding Author Email:** l.boukarana@univ-boumerdes.dz - **ORCID :** 0009-0007-3753-4574

[2]Departement of Electromechanics, University of Mostfa Benboulaid – Batna2, 05000, Alegria.
Email: yassina.medghaghet@gmail.com - **ORCID :** 0009-0001-0950-1771

Article Info:

DOI: 10.22399/ijcesen.5324
Received : 08 April 2026
Revised : 18 June 2026
Accepted : 21 June 2026

Keywords

PV-STATCOM
FUZZY Logic Control
PI Controller
Photovoltaic System
NPC Inverter

Abstract:

This paper presents a simulation study of a combined photovoltaic–STATCOM (PV-STATCOM) system connected to a 25 kV medium-voltage grid. The system consists of an 800 kW photovoltaic power plant interfaced with the grid through a three-phase neutral-point-clamped (NPC) inverter. The inverter performs a dual function: injecting active power generated by the PV array and compensating reactive power to support grid voltage. Two control strategies are implemented and compared: a conventional proportional–integral (PI) controller and a fuzzy logic controller (FLC). Their performance is evaluated in terms of DC-bus voltage regulation, reactive power compensation, and dynamic response under varying irradiation and load conditions. Simulation results show that the PV-STATCOM concept improves power quality and grid stability. In addition, the fuzzy logic controller provides faster dynamic response and better robustness compared with the conventional PI controller.

1. Introduction

The rapid growth of renewable energy integration in electrical power systems has introduced new challenges related to voltage regulation, power quality, and grid stability. Photovoltaic (PV) systems are among the most widely deployed renewable energy technologies. However, the intermittent nature of solar generation may cause fluctuations in power injection and voltage disturbances in the distribution network.

To address these issues, modern PV inverters are increasingly designed to provide ancillary services in addition to active power generation. One promising concept is the photovoltaic static synchronous compensator (PV-STATCOM), in which the grid-connected inverter operates both as a power converter for PV generation and as a reactive power compensator [1, 2].

In a PV-STATCOM system, the inverter injects active power into the grid during daytime operation while simultaneously regulating reactive power to improve voltage stability and power factor. During periods of low irradiation or night operation, the inverter can operate exclusively as a STATCOM, thus maximizing the utilization of the installed converter capacity.

Several studies have investigated PV-STATCOM systems for improving grid performance. Nevertheless, the effectiveness of the control strategy remains a key factor in achieving stable and reliable operation, especially under rapidly changing environmental conditions. Conventional PI controllers are widely used due to their simplicity, but their performance may degrade when dealing with nonlinear systems and uncertainties.

Intelligent control techniques such as fuzzy logic control (FLC) have therefore attracted significant attention in power electronics applications. Fuzzy controllers can handle nonlinearities and uncertainties more effectively than traditional controllers and may provide improved dynamic response [3, 4, 5].

The main contributions of this work are summarized as follows:

- Development of a detailed simulation model of an **800 kW PV-STATCOM system connected to a 25 kV medium-voltage grid**.
- Implementation of two control strategies (PI and fuzzy logic controllers) for reactive **power compensation and DC-bus voltage regulation.**

- Evaluation of controller performance under **different irradiation levels and load conditions.**
- Analysis of the **dual operating capability of the inverter**, including active power injection and STATCOM operation.

The remainder of this paper is organized as follows. One section describes the structure of the grid-connected PV system, followed by a section presenting the modeling of the PV generator and power converters. Another section details the control strategies, while a subsequent section discusses the simulation results and provides a comparative analysis. Finally, the paper concludes with a summary of the main findings. The PV-STATCOM system is illustrated in Figure 1.

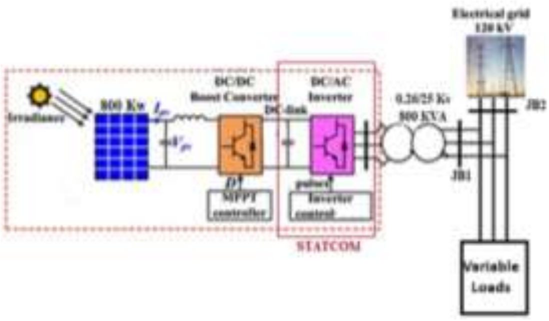

Figure 1. *PV-STATCOM system.*

2. Structure of a photovoltaic system

A grid-connected photovoltaic system generally consists of a PV generator, a DC-DC converter, a DC link, and a grid-connected inverter. The PV generator converts solar irradiation into electrical energy. Because the output voltage and power of the PV array vary with environmental conditions, a DC-DC converter is typically used to regulate the operating point of the generator.

In the proposed system, the PV generator is connected to a boost converter controlled by a maximum power point tracking (MPPT) algorithm. The converter adjusts the duty cycle to ensure that the PV array operates at its maximum power point.

The DC bus links the boost converter to the inverter and acts as an energy buffer. A three-phase NPC inverter then converts the DC voltage into AC voltage synchronized with the grid. A coupling transformer and filter are used to connect the inverter to the medium-voltage network [6, 7]. Figure 2 shows Three-phase structure of a grid-connected photovoltaic system.

3. Modelling of a photovoltaic generator

A photovoltaic cell can be modeled using an equivalent electrical circuit consisting of a current source, a diode, a series resistance, and a shunt resistance. The output current of the PV cell is given by the well-known nonlinear equation derived from the diode model.

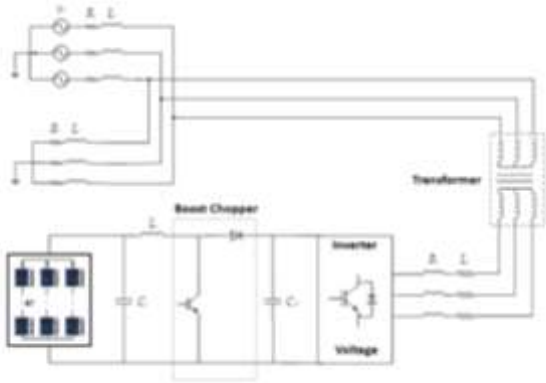

Figure 2. *Three-phase structure of a grid-connected photovoltaic system.*

To obtain higher output power, several cells are connected in series and parallel to form modules and arrays. In this study, the PV system uses modules rated at 315 W. The PV array configuration consists of series-connected modules forming strings, which are then connected in parallel to achieve the desired power level.

The PV array is designed to deliver a maximum power of approximately 800 kW under standard test conditions.

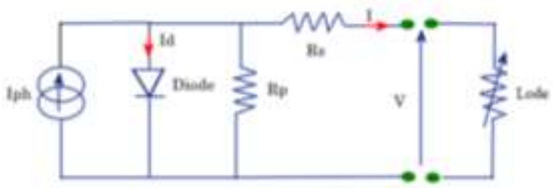

Figure 3. *Equivalent PV cell diagram.*

To generate higher power, multiple solar cells are assembled into a module. Typically, individual cells are connected in series (commonly 36 or 72 cells) to achieve the desired output voltage. Connecting modules in series increases the total voltage for a given current, while parallel connections increase the current at a constant voltage. To further enhance power output, modules are often interconnected in both series and parallel configurations, forming a photovoltaic array. Figure 3 shows the typical equivalent circuit of a photovoltaic cell [8].

As illustrated in Figure 3, a photovoltaic cell consists of a series resistor R_S and a shunt resistor R_P, both of which influence the cell's I–V characteristic.

- **Series resistance (R_S)** represents the internal resistance of the cell, primarily determined by the resistance of the semiconductor material, the contact resistance of the collector electrodes, and the resistivity of the electrodes [9, 10].

- **Shunt resistance (R_P)** is associated with leakage currents at the PN junction and depends on the fabrication process.

The behavior of a PV cell with a silicon-based PN junction can be described by the following equations (1) and (2):

$$I = I_{ph} - I_d - I_p \quad (1)$$

$$I = I_{sc}\left(\frac{G}{1000}\right) - I_0\left[exp\left(\frac{V+IR_S}{nV_T}\right) - 1\right] - \frac{V.IR_S}{R_P} \quad (2)$$

With:

- **I :** The current supplied by the cell.
- **Iph:** The illuminance-dependent photo-current (G). This current also corresponds to the short-circuit current.
- **Id:** The current flowing through the diode.
- **Ip:** Current diverted by the parallel resistor.
- **I_0:** The reverse saturation current of a diode.
- $\mathbf{V_T = \frac{K_T}{e}}$ **:** Thermal voltage.

In order to facilitate the modeling of a photovoltaic panel in the MATLAB environment, it is necessary to obtain the technical data of the unit module, specifically the individual cells. The module datasheet, which contains 96 cells and is identified as the SUNPOWER SPR-315E-WHT-D, can be accessed online. The following table summarizes the electrical characteristics of the photovoltaic module:

Table 1. *SUNPOWER SPR-315E-WHT-D solar module specifications*

Temperature (Tref)	**25 °C**
Eclairage (Eref)	1000 W/m2
Open circuit voltage (Vco)	64.6 V
Courant du court-circuit (Ics)	6.14 A
Maximum power point voltage (Vm)	54.7 V
Maximum power point current (Im)	5.76 A
Maximum power (Pm)	315 W

Our photovoltaic (PV) field consists of 64 modules connected in parallel, with 5 modules connected in series per string. Each module has a nominal voltage of 54.7 V and a nominal current of 5.76 A. Accordingly, the electrical characteristics of a solar panel can be expressed as shown in equation (3):

$$\begin{cases} V_{pv} = 5 \times 54.7 = 273.5V \\ I_{PV} = 64 \times 5.76 = 368.64\ A \\ P_{PV} = 320 \times 315 = 100\ kW \end{cases} \quad (3)$$

The complete system consists of 8 solar panels connected in parallel, resulting in a total installed power given by the following equation (4):

$$P_{TPV} = 8 \times P_{PV} = 800KW \quad (4)$$

4. Power conversion system

4.1. DC-DC step-up converter

DC-DC converters, also known as ‘choppers’, play a crucial role in solar power systems by adapting the variable-amplitude DC output voltage from a photovoltaic (PV) panel to the requirements of the load, which generally requires a constant DC voltage. In this section, we examine the most commonly studied DC voltage-boosting circuit: the boost converter, also known as a voltage-boosting/current-reducing circuit. A schematic of a boost chopper is shown in Figure 4 [11].

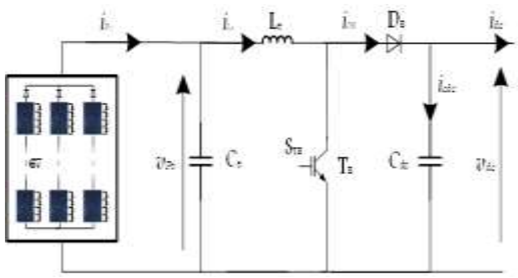

Figure 4. *Diagram of a boost chopper.*

The present study is based on the following assumptions:

- The supply voltage $v_{PV}$is assumed to be perfectly continuous and constant.
- The DC bus capacitor $C_{dc}$is considered sufficiently large so that the output voltage v_{dc}can be treated as continuous and constant.
- All components are assumed to be ideal.

4.2. MPPT control

In a photovoltaic system, which consists of a PV source and a load, identifying the optimum operating point using optimization techniques is a crucial step. This control strategy is commonly referred to in the literature as Maximum Power Point Tracking (MPPT) [12].

Integrating MPPT control with an intermediate adaptation stage enables the PV generator to operate optimally, ensuring the continuous extraction of maximum power. Regardless of prevailing weather conditions (temperature and irradiation) or the load, the control of the matching stage positions the system at the maximum power point (V_{MPP}, I_{MPP}).

Figure 5 illustrates a basic photovoltaic conversion chain with MPPT control. To simplify the operating conditions for this control, a DC load is used. As shown in this chain, MPPT control is inherently linked to a DC-DC converter, ensuring that the power delivered by the PV field corresponds to the maximum power (P_{MPP}) generated and allowing its direct transfer to the load [13].

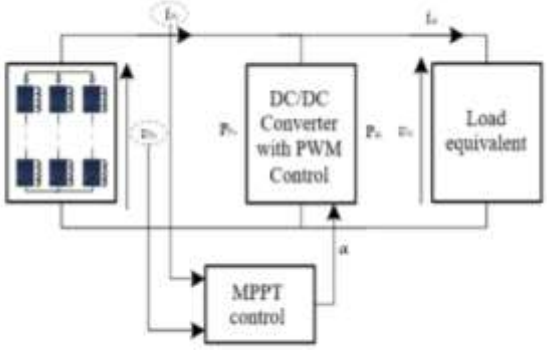

Figure 5. *Basic photovoltaic conversion chain with MPPT control.*

The control technique commonly used involves automatically adjusting the duty cycle, ensuring that the generator operates at its optimum capacity, regardless of weather conditions or sudden changes in load [14, 15].

Several MPPT control methods have been developed, incorporating algorithms of varying complexity to meet different requirements for accuracy and response speed. Some systems offer high accuracy but operate relatively slowly, whilst others allow for faster response times at the expense of efficiency. Power maximisation methods can generally be classified into two categories: indirect and direct.

4.3. The 'Disturb and Observe' (D&O) method

The P&O (Perturb and Observe) MPPT algorithm works by gradually adjusting the photovoltaic voltage V_{pv} and analysing the resulting response in photovoltaic power P_{pv}. This process allows the operating point to be steered towards the maximum power point [16].

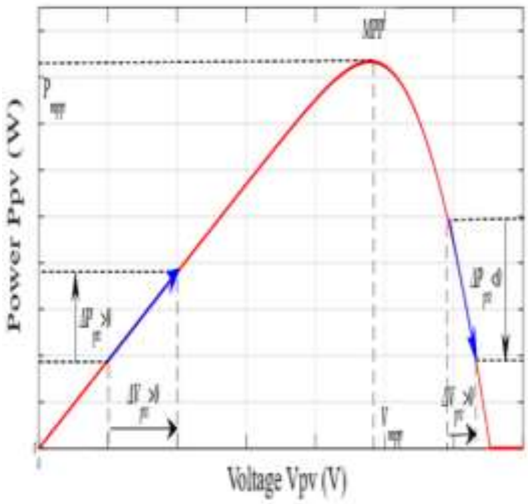

Figure 6. *Operating characteristics of the P&O method.*

As shown in Figure 6, across different operating ranges, an increase in the photovoltaic voltage V_{pv} leads to an increase in the photovoltaic power P_{pv}, indicating that the operating point lies to the left of the maximum power point (MPP). Conversely, if the output power decreases, the system has passed the MPP. This reasoning applies in a similar way when the voltage decreases. Analyzing the impact of voltage variations on the characteristic curve $P_{PV}(V_{PV})$ allows the operating point to be identified relative to the MPP. This then enables the system to converge towards maximum power through the implementation of an appropriate control strategy. The following four cases are presented by way of illustration [17]:

a. First case: $\Delta P_{Pv} > 0$ and $\Delta V_{Pv} > 0$

In this case, the operating point is located to the left of the maximum power point (MPP). Furthermore, the positive voltage variation (ΔV_{Pv}) indicates that the system is moving in the correct direction. In the next iteration, the PV field voltage should be increased, which can be achieved by decreasing the duty cycle. Consequently, the sequence of values is such that α(k) = α(k−1).

b. Second case: ΔPPv > 0 and ΔVPv < 0

Here, the operating point is located to the right of the MPP. The negative voltage variation (ΔV_{Pv}) indicates that the search for the MPP is proceeding in the correct direction. Therefore, in the next iteration, the voltage should be decreased (increasing the duty cycle), and the sequence of values can be expressed as: α(k) = α(k−1) + Δα.

c. Third case: ΔPPv < 0 and ΔVPv < 0

In this scenario, the operating point is to the left of the MPP, and the negative voltage variation (ΔV_{Pv}) shows that the system is moving in the wrong direction. To correct this, the voltage should be increased in the subsequent iteration. The sequence of values is then given by: α(k) = α(k−1) − Δα, where Δα is the step increment.

d. Fourth case: ΔPPv < 0 and ΔVPv > 0

Here, the operating point is to the right of the MPP, and the positive voltage variation (ΔV_{Pv}) indicates that the system is moving in the wrong direction. In the next iteration, the voltage should be decreased, which increases the duty cycle. The sequence of values is expressed as: α(k) = α(k−1) + Δα.

As illustrated in Fig.7, the P&O MPPT control algorithm analyzes the evolution of power following each voltage perturbation. To determine the PV field power at each instant, two sensors (for PV field current and voltage) are required. Through the operation of this algorithm, the PV voltage V_{PV} is perturbed at each MPPT cycle.

Upon reaching the MPP, V_{PV}oscillates around the ideal operating voltage V_{MPP}. This phenomenon leads to a slight power loss, the magnitude of which depends on the step size of the perturbation [18].

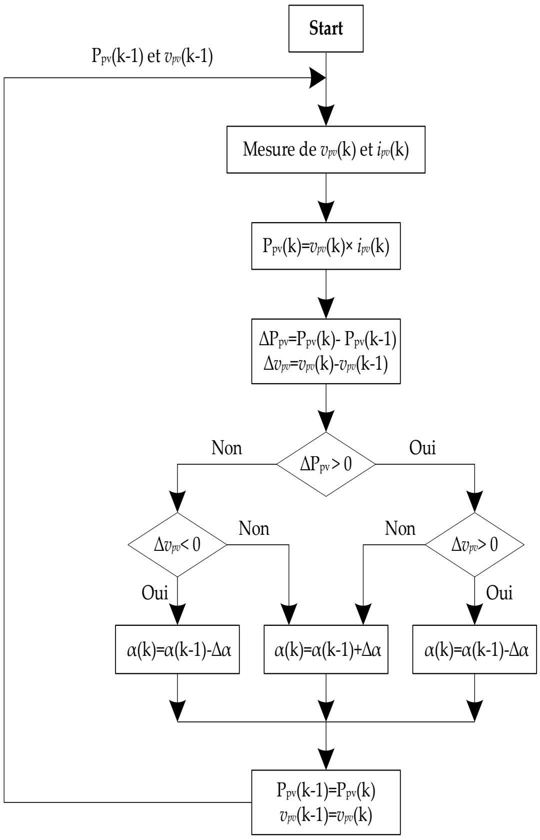

Figure 7. *Flowchart of the perturbation and observation algorithm.*

4.4. NPC three-level inverter

Figure 8 illustrates the general structure of the three-level floating-diode inverter, also known as a locked-neutral-point (LNP) inverter. This structure comprises two identical capacitors whose common midpoint is designated ‘o’, enabling the inverter to achieve an additional voltage level compared to the conventional two-level inverter [19].
Under normal operating conditions, the total DC bus voltage Vdc is distributed evenly between the two capacitors, resulting in a voltage of Vdc/2 across them (this assumption is used in this section). The output is connected to a symmetrical three-phase load connected in a star configuration with an isolated neutral. The inverter consists of three branches: a, b and c. Each branch comprises four fully controllable switches (Kx1, Kx2, Kx3 and Kx4, where x denotes the branch index) connected in series, in anti-parallel with four main diodes to ensure current reversibility in the load, as well as two blocking diodes (Dx1 and Dx2) connected to the centre of the DC bus.

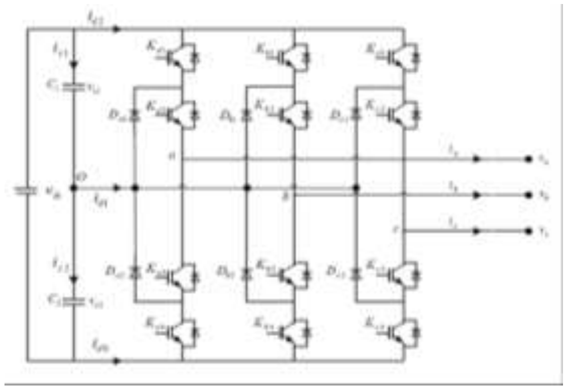

Figure 8. *Power structure of the NPC three-phase three-level inverter.*

Figure 9 illustrates the configuration of a three-level NPC inverter branch.

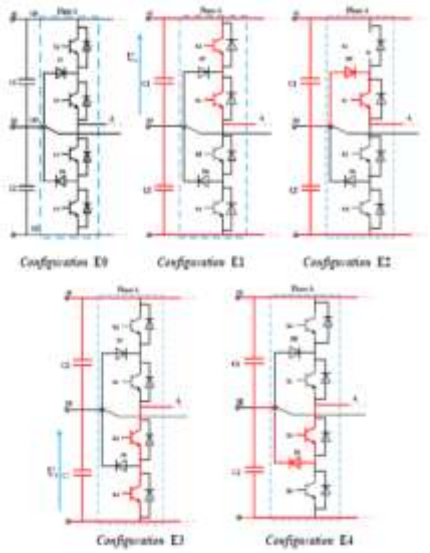

Figure 9. *Different possible electrical configurations of a three-level inverter.*

4.5. Conventional PWM without injection of the three harmonics, using two unipolar carriers

The drive signals for one arm of the drive are determined by comparing two triangular waveforms with a sinusoidal reference. The two waveforms are defined by the following equations:

$$U_{p1} = \begin{cases} 2U_{p\,max}\frac{t}{T_p}\ ; \text{pour } 0 \le t \le \frac{T_p}{2} \\ 2U_{p\,max}\left(-\frac{t}{T_p}+1\right); \text{pour } \frac{T_p}{2} \le t \le T_p \end{cases} \quad (5)$$

And:

$$U_{p2} = U_{p1} - U_{p\,max} \quad (6)$$

The algorithm used to implement this modulation technique is as follows:

$$\begin{cases} \text{if } (V_{\text{réfk}} > U_P)\ \&\ (V_{\text{réfk}} > U_{P2}) \text{then } S_{k1} = 1 \\ \text{else } S_{k1} = 0 \end{cases} \quad (7)$$

With: $S_{k2} = \overline{S}_{k1}$

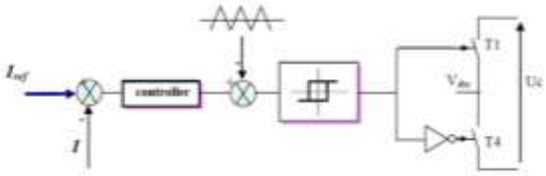

Figure 10. *PWM control of the inverter.*

4.6. Connection filter

The installation of an inductive filter, strategically positioned between the drive and the mains supply, is a crucial aspect of the system design. The main purpose of this filter is to generate near-sinusoidal currents, thereby ensuring the stability and efficiency of the entire system. The first-order filter fulfils two main functions: it attenuates high-frequency harmonics and facilitates current control. Furthermore, it helps to reduce voltage fluctuations at the connection point. The inductance is sized based on the maximum current ripple, assuming a no-load condition and negligible resistance [20, 21].
Where:

- $\boldsymbol{V_r}$: Modulated RMS voltage at the inverter output [V]
- $\boldsymbol{I(t)}$: Current flowing to the grid [A]
- $\boldsymbol{L}$: Inverter output inductance [H]

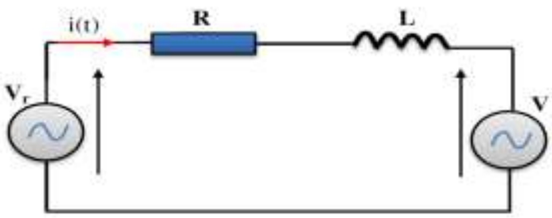

Figure 11. *Simplified network connection diagram.*

The three-phase network consists of three sinusoidal voltages of the same frequency, phase-shifted by 2π/3 radians and having identical rms values, thus forming a balanced three-phase system. The voltage of a balanced three-phase electrical system can be expressed as follows (Equation 8) [22, 23]:

$$\begin{cases} V_a = V_m \cos \omega t \\ V_b = V_m \cos(\omega t - \frac{2\pi}{3}) \\ V_b = V_m \cos(\omega t + \frac{2\pi}{3}) \end{cases} \quad (8)$$

5. Control strategy

5.1. Control using standard PI controllers

5.1.1. Control of the DC bus

To achieve these control objectives, a controller has been designed. On the one hand, it is used to track power setpoints under normal operating conditions, with parameters generally defined by the electricity network operator. On the other hand, it is essential to monitor electrical parameters in the event of a fault.
It is crucial to maintain the DC voltage V_{dc} across the DC bus at a constant level. Voltage fluctuations must be minimised in order to prevent the voltage limits of the semiconductor switches from being exceeded and to avoid any degradation in the inverter's performance. To regulate the DC voltage, a dedicated controller is required [24].

The Laplace transform of the DC voltage V_{dc} is given by equation (9):

$$V_{dc}(p) = \frac{1}{C_{eq}p} i_{ceq}(p) \quad (9)$$

To obtain the i_{Ceq} signal, either a proportional (P) controller or a proportional-integral (PI) controller can be used. The latter is often considered the preferred choice, as it effectively eliminates steady-state error.
The DC voltage control unit is shown in the diagram in Figure 12.

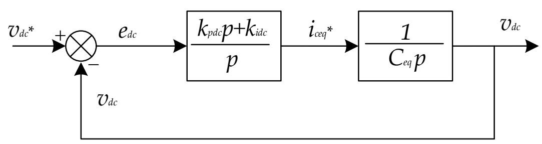

Figure 12. *DC voltage check.*

The corresponding open-loop transfer function in equation (10):

$$F_{dc}(p) = \frac{k_{pdc}p + k_{idc}}{p} \frac{1}{C_{eq}p} \quad (10)$$

The closed-loop transfer function of equation (11):

$$H_{dc}(p) = \frac{k_{pdc}p + k_{idc}}{C_{eq}p^2 + k_{pdc}p + k_{idc}} \quad (11)$$

It is necessary to draw an analogy between the characteristic equation of the function $H_{dc}(p)$ and the transfer function of a second-order closed-loop system, which is expressed by the following equation (12):

$$G_{dc}(p) = p^2 + 2\xi_{dc}p + \omega_{ndc}^2 \quad (12)$$

The values of the controller constants are therefore determined as follows, based on equation (13):

$$\begin{aligned} k_{pdc} &= 2\xi_{dc}\omega_{ndc}C_{eq} \\ k_{idc} &= C_{eq}\omega_{ndc}^2 \end{aligned} \quad (13)$$

Ultimately, the values KP = 7 and Ki = 800 are obtained from equation (10).

5.1.2. Control of currents Id and Iq

The proportional-integral (PI) controller is the most commonly used controller for current control due to its simplicity. The corresponding transfer function is given by equation (14):

$$R(p) = \frac{k_P p + k_I}{p} \quad (14)$$

With:
- **p:** Laplace operator.
- **KP** and **Ki:** Designate the controller gains.

After compensation, the simplified diagram of the current control loop is shown in Figure 13.

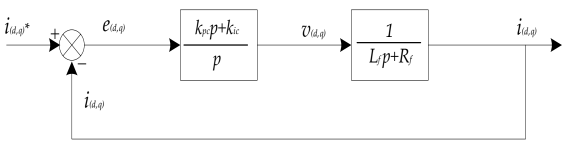

Figure 13. *Current regulation.*

The corresponding open-loop transfer function is given by equation (15):

$$F(p) = \frac{k_{pc}p + k_{ic}}{p}\frac{1}{L_f p + R_f} \quad (15)$$

The closed-loop transfer function is given by equation (16):

$$H(p) = \frac{k_{pc}p + k_{ic}}{L_f p^2 + (R_f + k_{pc})p + k_{ic}} \quad (16)$$

To ensure the closed-loop system operates correctly, it is essential to select the coefficients k_{pc} and k_{ic} carefully. In the pole-placement method, an analogy must be drawn between the characteristic equation of the function H(p) and that of a second-order closed-loop system, as expressed by the following equations (17) and (18):

$$G(p) = p^2 + 2\xi_c\omega_{nc}p + \omega_{nc}^2 \quad (17)$$

$$G(p) = p^2 + 2\xi_c\omega_{nc}p + \omega_{nc}^2 \quad (18)$$

The values of the controller constants are therefore obtained as follows, based on equation (19):

$$\begin{aligned} k_{pc} &= 2\xi_c\omega_{nc}L_f - R_f \\ k_{ic} &= L_f\omega_{nc}^2 \end{aligned} \quad (19)$$

With:
- ξ_c and ω_{nc}: Represent the damping factor and pulsation of the second-order system, respectively.
- K_{pc} and K_{Ic}: PI controller gains of active and reactive currents.

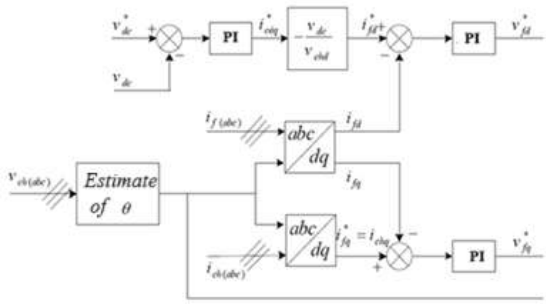

Figure 14. *Control diagram.*

In the end, the values are set at KP = 0.3 and Ki = 20.

5.2. Control via a fuzzy logic controller (FLC)

The general principles and fundamental theory of fuzzy logic incorporate aspects of possibility theory, which uses fuzzy sets to characterise the various variables within the system to be controlled. Fuzzy reasoning is applied through a set of rules established on the basis of human expertise, which can be manipulated to generate appropriate commands or decisions. The main elements of the basic theory of fuzzy logic are [25, 26]:

- Linguistic variables and fuzzy sets
- Membership functions
- Operators
- Fuzzy inference
- Mamdani-type controllers

In the following discussion, the focus is on the Mamdani-type fuzzy controller, which is the most widely used type. This controller has been applied in a fuzzy control context [27] and takes the following general form for N_x inputs:

R_k:if x_1 is A_{1k} and ... and x_{N_x} is $A_{N_x k}$ then y is B_k

A block diagram of this type of controller is shown in Figure 15. In many cases, fuzzy control involves the use of input variables that include the deviation e between the controlled variable and its reference value, as well as its change Δe. The 'min' operator is used for 'and' and 'then' implications, whilst the 'max' operator is used for 'or' rule aggregation. The resulting inferences are called 'min-max'.

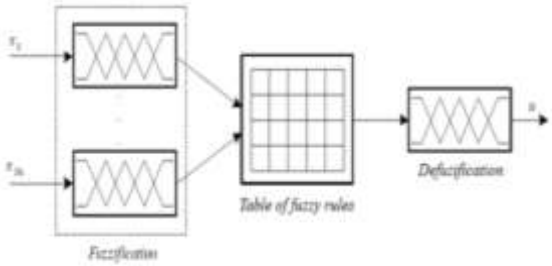

Figure 15. *Controller of Mamdani*

5.3. Characteristics of the fuzzy controller used

The main characteristics of the fuzzy controller used in this study are as follows [28]:
Fuzzification with a continuous domain ranging from -1 to 1.
Inference using Mamdani's min-max method.
Seven fuzzy sets for the error and its variation, defined by triangular membership functions, with the parameters: a=0.25, b=0.5, c=0.75; x∈ [-1,1], representing either e_f or Δe_f.

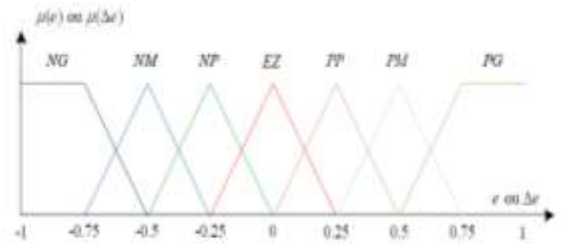

Figure 16. *Distribution of selected membership functions.*

Table 2 presents the fuzzy rules used to design this controller. The number of parameters to be set is considerable (7 × 7 = 49 parameters). Therefore, the controller primarily focuses on the degrees of freedom associated with the membership functions of the input and output variables, which have a global influence on the system. This approach effectively reduces the number of variables within the controller. The block diagram of the fuzzy control structure of a PV-STATCOM is shown in Figure17.

6. Simulation result

6.1. Characteristics of the three-level inverter

The control signals for an inverter arm using a conventional PWM without injection of the third harmonic with two triangular unipolar carriers are determined by comparing two triangular carriers and a sinusoidal reference, figure (18).

Table 2. *Table of fuzzy rules*

		e						
		NG	NM	NP	EZ	PP	PM	PG
Δe	NG	NG	NG	NG	NG	NM	NP	EZ
	NM	NG	NM	NM	NM	NP	EZ	PP
	NP	NG	NM	NP	NP	EZ	PP	PP
	EZ	NM	NM	NP	EZ	PP	PM	PM
	PP	NP	NP	EZ	PP	PP	PM	PM
	PM	NP	EZ	PP	PM	PM	PM	PG
	PG	EZ	PP	PM	PG	PG	PG	PG

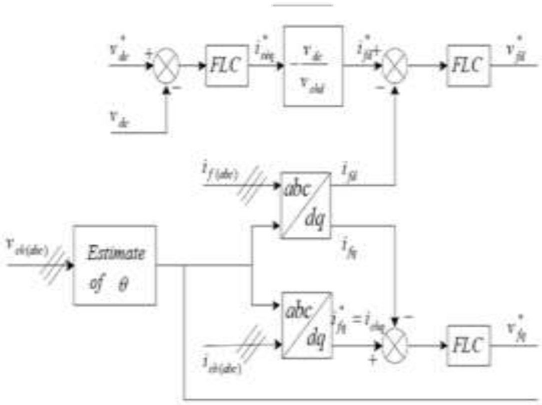

Figure 17. *Fuzzy PI control.*

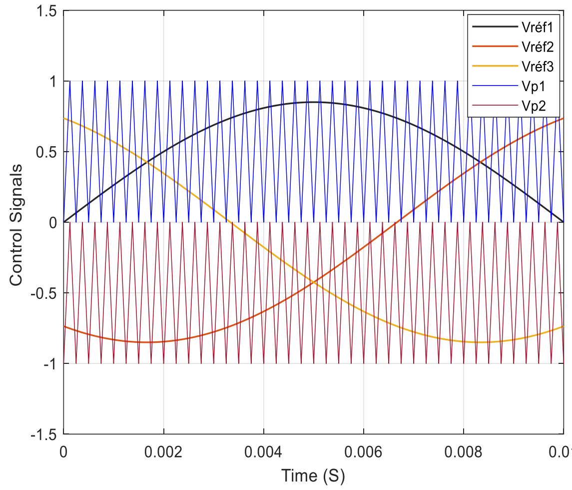

Figure 18. *Principle of PWM control with two unipolar carriers.*

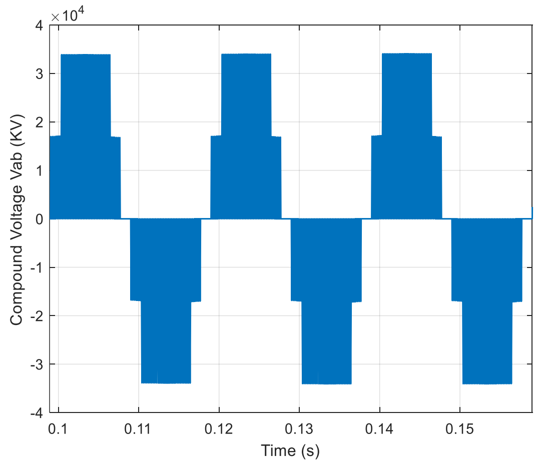

Figure 19. *Compound voltage Vab for r = 0.85 and m= 40*

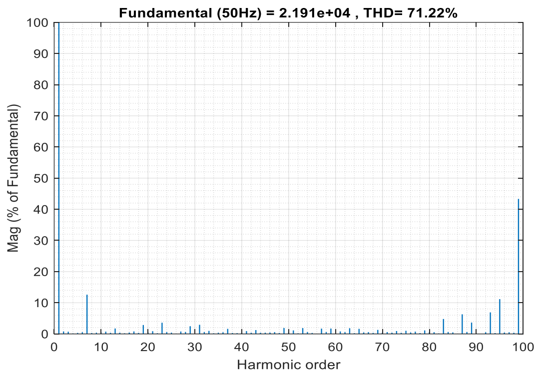

Figure 20. *Harmonic spectrum of Vab.*

Figure 19 and Figure 20 show the composite voltage at the output of the STATCOM inverter. The four levels (E, E/2, -E/2, E) of the composite voltage can be seen, as well as the harmonic spectrum with a harmonic distortion rate of 71.22% for a regulation coefficient (r = 0.8) and a frequency modulation index (m = 40). It should be noted that for a conventional two-level inverter, the THD% is around double, which is an advantage of the chosen structure.

6.2. Influence of switching frequency on phase current

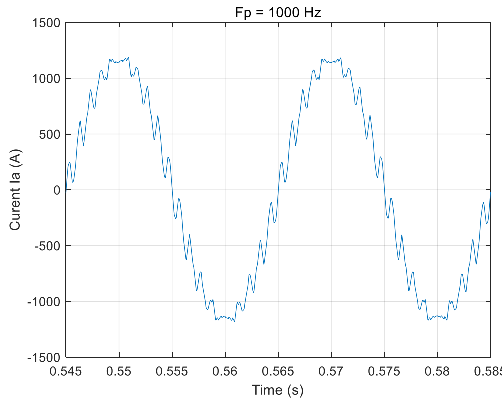

Figure 21. *Current (Ia) for Fp = 1000Hz.*

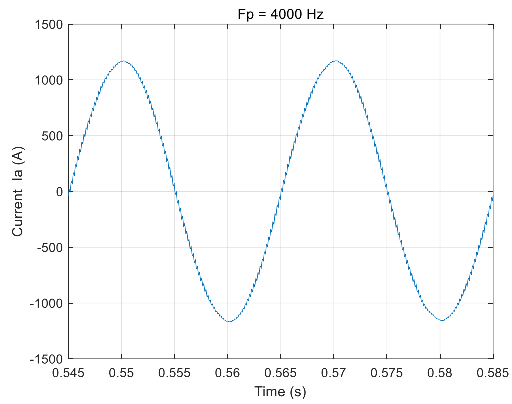

Figure 22. *Current (Ia) for Fp = 4000Hz*

Figure 21 and Figure 22 show the STATTCOM output current for two carrier frequencies (1khz, 4khz). It can be seen that the higher the frequency, the lower the current ripple and the closer the current is to sinusoidal. However, this frequency is limited by the application and the technology of the power switches.

6.3. Rate of harmonic distortion

The rate of harmonic distortion (Total Harmonic Distortion: THD) is a measurement used to determine the alteration of a signal compared to a purely sinusoidal signal.

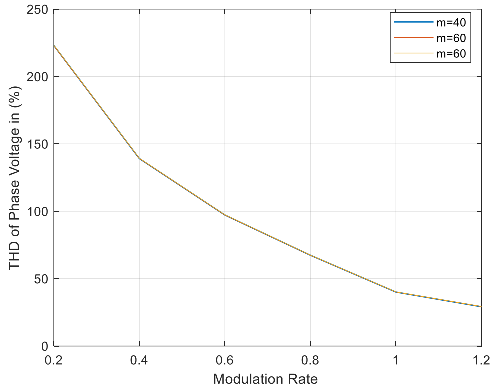

Figure 23. *Phase voltage harmonic distortion rate.*

Increasing the modulation index pushes the harmonics towards higher frequencies. However, Figure 23 shows that this increase does not alter the rate of harmonic distortion, which instead decreases as a function of the increase in the modulation ratio.

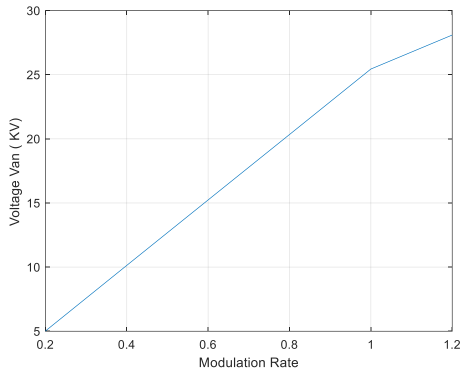

Figure 24*. Setting characteristic for m=40.*

From figure 24, it can be deduced that the modulation rate allows linear adjustment of the amplitude of the fundamental in the range r ϵ [0, 1]. The use of three-level inverters for the application of STATCOM seems to be a fairly interesting solution. This figure shows that:

- Increasing the modulation ratio (r = 0...1.2) reduces the THD.
- Increasing the modulation ratio r increases the number of harmonics in a family and at the same time reduces their amplitude.

The variation in the amplitude of the fundamental harmonic does not depend on the variation in the modulation index m.

6.4. PV-STATCOM system operating modes

The PV-STATCOM system is connected to the grid via a transformer substation with a nominal power rating of $S = 800$ kVA, which must not be exceeded under any circumstances. Three modes of operation can be distinguished:

- **Full irradiation mode:** The PV plant delivers its maximum power of 800 kW, corresponding to the transformer substation limit. In this case, the STATCOM function is disabled, and the inverter injects only active power into the grid: $P_{inj} = 800\ Kw, Q_{inj=0}$.
- **Partial irradiation mode:** If the plant delivers less than its rated power (800 kW), the inverter can operate as a STATCOM to compensate for part of the reactive power flowing in the grid transmission lines, while remaining within the limits of the transformer substation:

$$\sqrt{P_{inj}^2 + Q_{inj}^2} \leq 800KVA \quad (20)$$

- **Night mode:** If there is no irradiation (at night) and the PV plant is no longer injecting active power, the inverter can operate as a STATCOM at maximum capacity: $P_{inj} = 800\ Kw, Q_{inj=0}$.

For the remainder of this study, the behavior of the power device will be analyzed through simulation for a variable load, a constant temperature of 25 °C, and different irradiation levels: 1000 W/m², 500 W/m², and 0 W/m².
For each scenario, the following will be presented:

- The power injected by the PV-STATCOM system.
- The power injected into or absorbed by the power grid.
- The power factor at the grid busbar.

6.5. Irradiation profile

Figure 25 illustrates the profile of the variable irradiation. The irradiation profile consists of three modes:

- **Mode 1:** [0, 0.6 s]; $I_r = 1000$ W/m²
- **Mode 2:** [0.6, 1.2 s]; $I_r = 500$ W/m²
- **Mode 3:** [1.2, 2 s]; $I_r = 0$ W/m²

6.6.Variable load profile

Figure 26 illustrates the profile of an inductive variable load. The load operates at two levels:

- **Level 1:** [0, 1s]: Pc = 500 Kw, Qc = 400 KVar.
- **Level 2:** [1, 2s]: Pc = 1500 Kw, Qc = 1100 KVar.

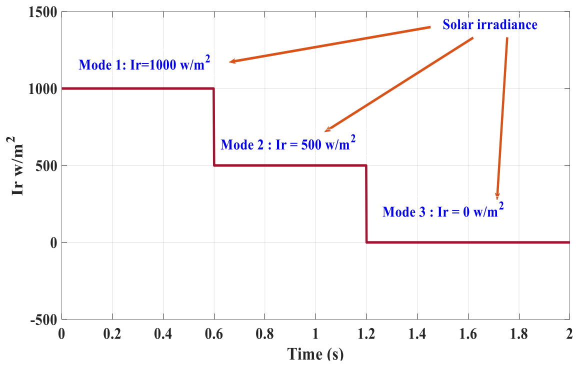

Figure 25. *Irradiation profile*

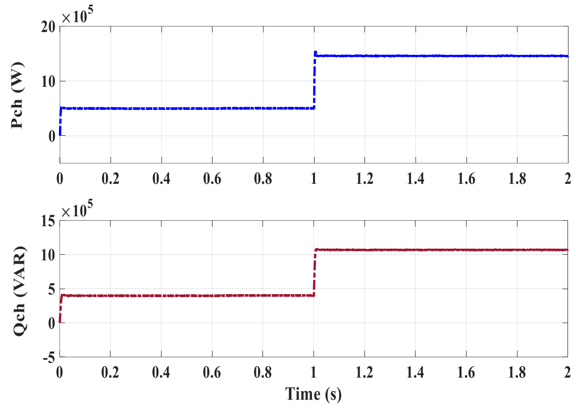

Figure 26. *Variable load profile (Active and Reactive Power).*

6.7.The power injected by the PV-STATCOM system

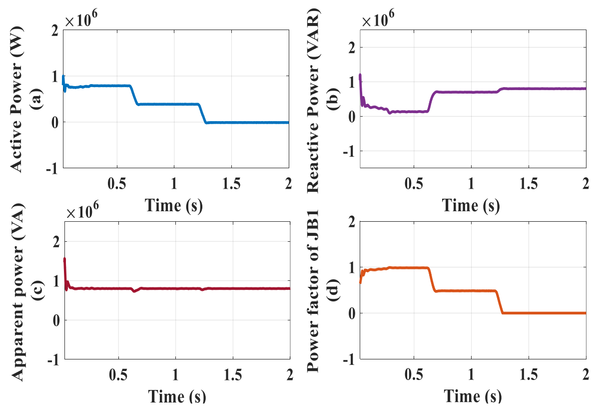

Figure 27. *PV-STATCOM power injections, with power factor.*

- **Mode 1: [0, 0.6 s];** $I_r = 1000$ W/m² The operation of the PV-STATCOM system is illustrated in Figure 27 (a) to Figure 27 (d). The power injected into the grid is slightly lower than the power generated by the PV array due to losses in the conversion chain. The STATCOM supplies only a small amount of capacitive reactive power, since the active power is close to the transformer nominal limit of 800 kW. The apparent power remains constant at 800 kVA, ensuring compliance with the imposed thermal constraints. Finally, the power factor at the point of connection (JB1) is close to unity, indicating efficient utilization of the system.

- **Mode 2: [0.6, 1.2 s];** $I_r = 500$ W/m² As shown in Figure 27 (a) to Figure 27 (d), a decrease in irradiance to 500 W/m² leads to a reduction in the active power injected, reaching approximately 400 kW. In response, the STATCOM increases the injected reactive power to about 700 kVAr, while respecting the transformer apparent power limit (800 kVA), as illustrated in Figure 27 (c). However, the power factor at the connection point (JB1) decreases to around 0.5 due to the reduced active power, in accordance with:

$$\sqrt{P_{inj}^2 + Q_{inj}^2} \leq 800 \text{ Kva} \quad (21)$$

- **Mode 3: [1.2, 2 s];** $I_r = 0$ W/m² As illustrated in fig.27, the PV plant no longer injects active power ($P_{inj} = 0$). Consequently, the system operates purely as a STATCOM, utilizing the full apparent power capacity of the transformer to inject reactive power ($Q_{inj} = 800$ kVAr) into the grid. This enables effective compensation of the reactive power in the transmission lines, as shown in Figure 27 (b). It should also be noted that the transformer operates continuously at its nominal apparent power ($S_n = 800$ kVA), as illustrated in Figure 27 (c).

6.8.Currents injected by PV-STATCOM

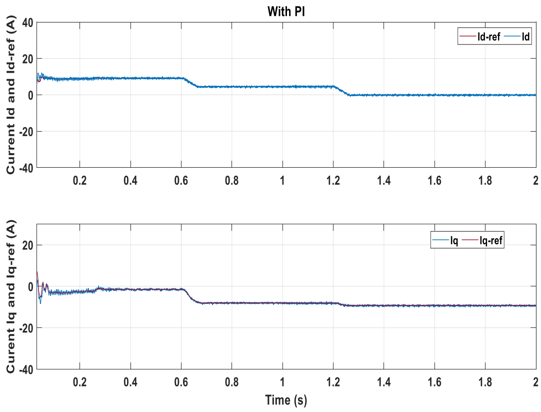

Figure 28. *The currents injected by the PV-STATCOM with PI*

As shown in Figure 28, the control currents of the PV-STATCOM system are presented. The active current (I_d) regulates the injected active power, while the reactive current (I_q) directly controls the injected reactive power.

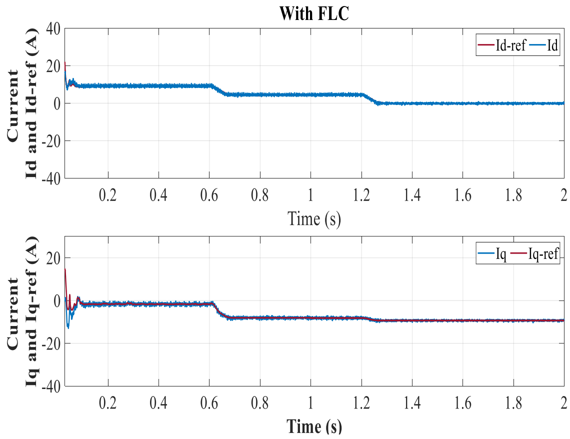

Figure 29. *The currents are injected by the PV-STATCOM with FLC.*

The FLC controller has been shown to excel in dynamic adaptation, providing effective disturbance rejection and precise setpoint tracking. These results confirm that fuzzy control is the optimal choice for current regulation.

Table (3) presents a comparative study between PI and FLC control current.

Table.3. *PI and FLC performance for current.*

	PI	FLC
1st Overrun (%)	1.20	1.01
2nd Overrun (%)	2.48	0
3rd Overrun (%)	2.05	0
Ripple rate(%)	2.64	0.71
Response time(s)	0.064	0.019

6.9. Vdc voltage

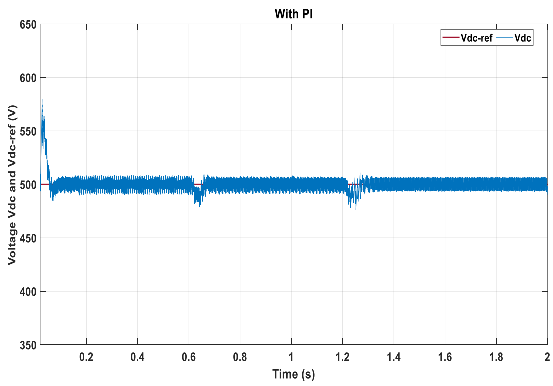

Figure 30. *Vdc voltage and its reference with a PI.*

As shown in Figure 30, the DC bus voltage (500 V) is effectively maintained, ensuring proper connection to the electrical network and confirming the effectiveness of the DC bus voltage control loop.

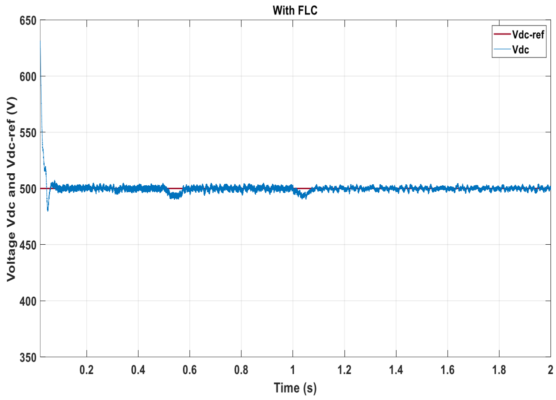

Figure 31. *Vdc voltage and its reference with an FLC.*

This Figure 31 highlights the effectiveness of fuzzy control (FLC) in stabilizing the DC voltage, owing to its ability to manage the non-linearities of the PV system and respond rapidly to variations. The FLC controller plays a key role in maintaining high bus voltage stability, ensuring a reliable connection to the electrical grid. These results confirm the accuracy of the DC voltage control loop design and emphasize the robustness and responsiveness of the fuzzy controller under dynamic conditions.
Table 4 presents a comparative analysis of the PI and fuzzy PI control strategies.

Table.4. *PI and FLC performances for vdc control*

Vdc	PI	Fuzzy PI
1st Overrun (%)	5.15	4.64
2nd Overrun (%)	1.91	0
3rd Overrun (%)	0.65	0
Ripple rate(%)	0.132	0.073
Response time(s)	0.2	0.122

The comparative analysis highlights the advantages of fuzzy control. The FLC offers faster response, reduced overshoot, and enhanced stability compared to the conventional PI controller. Additionally, the DC bus voltage remains more stable under dynamic operating conditions. These results demonstrate the effectiveness of intelligent control strategies for multifunctional PV inverters.

6.10. Power flow

As shown in Figure 32, the flow of different powers (injected by the PV-STATCOM system and supplied by the grid) is analyzed, distinguishing between two cases:

- **[0, 1 s]:** The electrical grid absorbs the surplus active power provided by the PV power plant; the negative sign indicates that the power is absorbed by the grid rather than injected. Regarding reactive power, the grid supplies reactive power to the load.

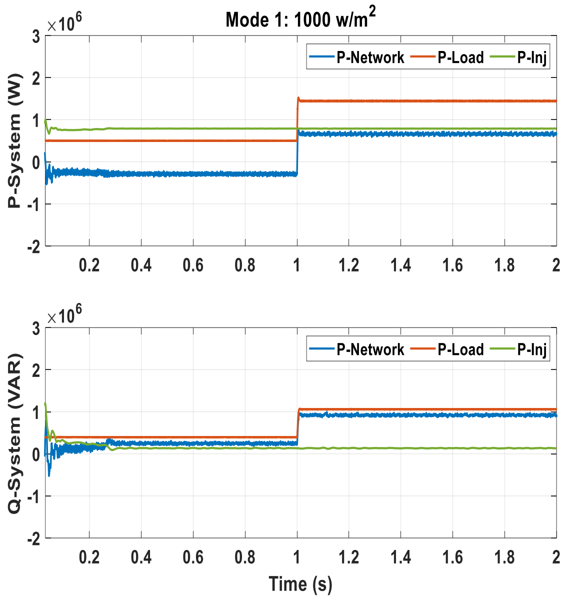

Figure 32. *Active and reactive power flow.*

- **[1, 2 s]:** As the load increases from 500 kW to 1500 kW, the grid injects active power to compensate for the shortfall in PV generation. Similarly, the reactive power required by the load is supplied by the electrical grid.

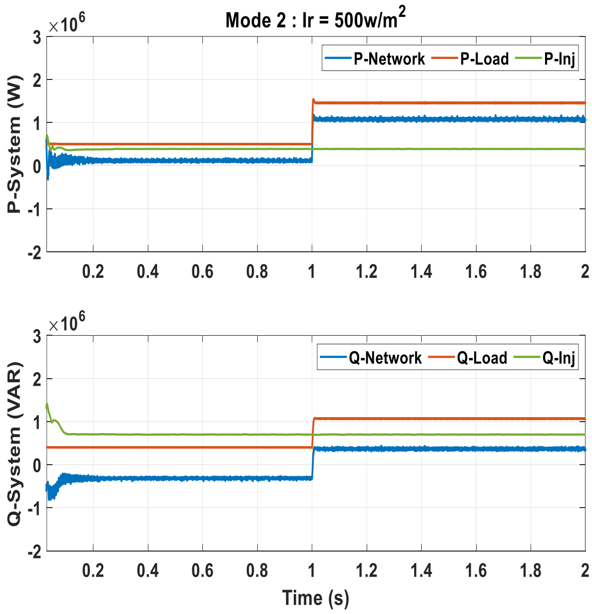

Figure 33. *Active and reactive power flow.*

As shown in Figure 33, the evolution of the different power flows (injected by the PV-STATCOM system and the electrical grid) is clearly observed.

- **[0, 1 s]:** The grid compensates for the lack of reactive power at the 500 kW load, as the PV plant can generate a maximum of only 400 kW. Meanwhile, the grid absorbs the surplus reactive power supplied by the STATCOM (100 kVAr).
- **[1, 2 s]:** The electrical grid provides the additional active power required by the 1500 kW load, since the PV plant continues to supply only

400 kW. Similarly, the grid supplies the remaining reactive power:

$$Q_{res} = Q_{ch} - Q_{inj} = 1100 - 700 = 500 \text{ kVAr}$$

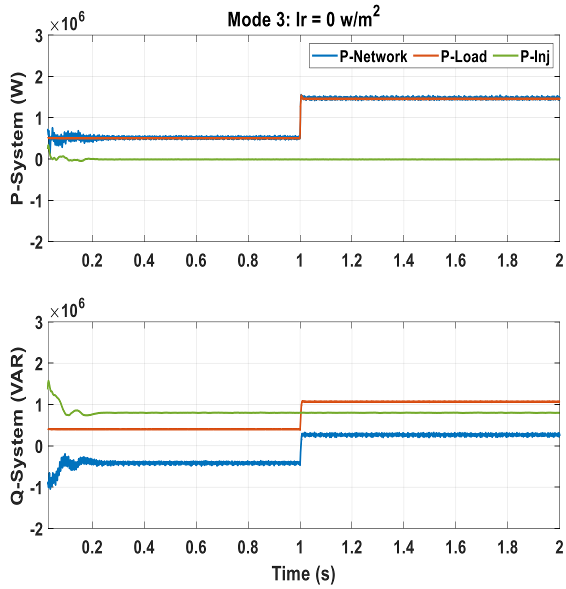

Figure 34. *Active and reactive power flow.*

Figure 34 provides a comprehensive illustration of the evolution of power flow, showing the contributions of both the STATCOM and the electrical network. The grid supplies all the active power to the load, even when the PV plant is not generating. Conversely, the grid absorbs the surplus reactive power injected by the STATCOM, thereby providing effective compensation for the reactive power of the transmission lines.

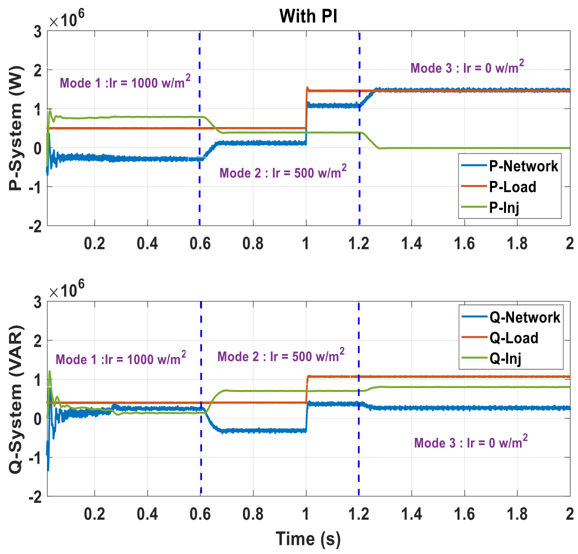

Figure 35. *Active and reactive power flow with PI.*

As illustrated in Figure 35, the exchange of active and reactive power between the PV-STATCOM system, the load, and the grid is described by the following power balance equations (22):

$$\begin{cases} P_{inj} + P_{res} + P_{ch} = 0 \\ Q_{inj} + Q_{res} + Q_{ch} = 0 \end{cases} \quad (22)$$

Furthermore, to ensure compliance with the thermal limits of the PV-STATCOM system transformer, the apparent power must satisfy:

$$\sqrt{P_{inj}^2 + Q_{inj}^2} \leq 800 \text{ kVA} \quad (23)$$

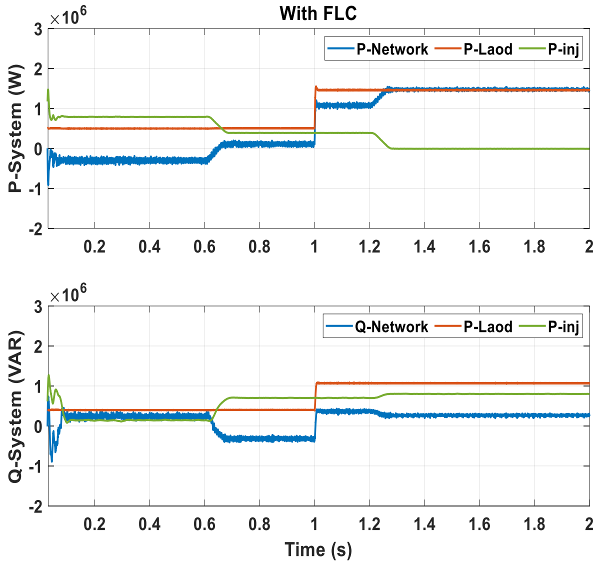

Figure 36. *Active and reactive power flow with FLC.*

As shown in Figure 36, the FLC controller enables a smooth and balanced exchange of active and reactive power between the PV-STATCOM system, the load, and the electrical grid. The adaptability of the FLC is a key factor in maintaining power balance while providing dynamic and precise regulation, even under variations in irradiation or load.

6.11. Power factor of (JB2)

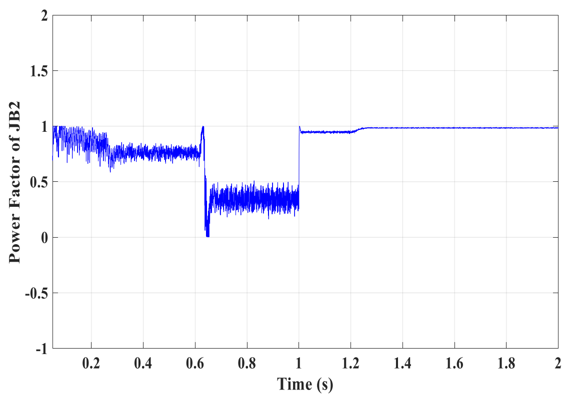

Figure 37. *Power factor of (JB2)*

Regarding the evolution of the power factor, observations at the busbar (JB2) of the electrical network reveal the following:

- During the interval [0, 0.6 s], the power factor is high, reaching approximately 0.85, indicating strong adaptability.
- In the interval [0.6, 1.25 s], the injected power decreases by 50%, resulting in a reduction of the power factor to 0.5.
- From 1.25 s onward, when irradiation drops to zero, the power factor reaches unity, providing effective compensation for the reactive power of the lines.

7. Comparative analysis between the PI and the FUZZY PI control strategies.

A comparative analysis of the PI and FLC controllers applied to the PV-STATCOM system highlights the superiority of the FLC in terms of performance, stability, and robustness. The FLC enhances the monitoring and regulation of active and reactive power, providing smoother and more continuous control under varying irradiation and load conditions.

In contrast, the PI controller exhibits overshoot and slower response times. The FLC reduces overshoot by approximately 5%, improves response time by up to 15%, and achieves faster disturbance rejection, typically 0.8 to 0.9 s earlier. Regarding DC bus voltage control, the FLC demonstrates greater stability and reacts more dynamically to voltage fluctuations, ensuring a reliable connection to the grid.

Moreover, the use of FLC improves equilibrium and stability in the power exchange between the PV-STATCOM system, the load, and the grid, maintaining adherence to the power balance constraints. Despite its increased design complexity, the FLC controller is highly adaptable to variable operating conditions and resilient to non-linearities, making it a more efficient and reliable solution compared to the conventional PI controller for modern PV systems.

8. Conclusion

This article focused on the analysis of a combined PV-STATCOM system connected to a medium-voltage (MV) grid:

- The PV power plant supplies active power to the electrical grid.
- The appropriately controlled inverter operates as a STATCOM, compensating for reactive power in the transmission lines while remaining within the transformer's apparent power limit (800 kVA).
- Simulation results under different irradiance levels and load conditions demonstrated the effectiveness of the PV-STATCOM system, highlighting two key operational scenarios:
  a. **Daytime operation:** The system supplies both active and reactive power, with a variable power factor, while respecting the thermal limits of the transformers. This imposes a safety margin, defining a maximum threshold for reactive power injection.
  b. **Nighttime operation:** The system functions as a pure STATCOM, injecting no active power, thereby fully utilizing the reactive power capacity of the transformer to compensate for the grid's reactive load.

A comparative study of two control strategies—PI (Proportional-Integral) and FLC (Fuzzy Logic Controller)—applied to the system's control loops yielded the following insights:

- The PI controller, while simple and widely used, exhibits limitations under fast disturbances, showing slower response times and reduced robustness to irradiation and load variations.
- The FLC controller provides superior dynamic stability, more accurate monitoring of currents and injected power, and more flexible adjustment without manual retuning. It also ensures better regulation of the DC bus voltage and stricter adherence to the system's power balance.
- However, the FLC is more complex to design, requiring the definition of fuzzy rules and nonconventional modeling approaches.

In conclusion, implementing the FLC as the control strategy in such hybrid PV-STATCOM systems significantly enhances overall performance, particularly under variable operating conditions typical of renewable energy sources.

Author Statements:

- **Ethical approval:** The conducted research is not related to either human or animal use.
- **Conflict of interest:** The authors declare that they have no known competing financial interests or personal relationships that could have appeared to influence the work reported in this paper

- **Acknowledgement:** The authors declare that they have nobody or no-company to acknowledge.
- **Author contributions:** The authors declare that they have equal right on this paper.
- **Funding information:** The authors declare that there is no funding to be acknowledged.

- **Data availability statement:** The data that support the findings of this study are available on request from the corresponding author. The data are not publicly available due to privacy or ethical restrictions.

References

[1] Z. Rashid, M. Amjad, and W. Anjum, "Indirect grid power factor tuning with PV STATCOM using shift mode phase locking strategy," *Electrical Engineering, vol. 105, no. 3, pp. 1317–1329, Apr. 2023.*

[2] K. Kouider and A. Bekri, "Enhancing transient stability and dynamic response of wind penetrated power systems through PSS and STATCOM cooperation," *Int. J. Renew. Energy Dev., vol. 12, no. 5, pp. 816–831, Sep. 2023.*

[3] M. Melhaoui et al., "Hybrid fuzzy logic approach for enhanced MPPT control in PV systems," *Scientific Reports, vol. 15, Art. no. 19235, 2025.*

[4] A. Boudia, S. Messalti, S. Zeghlache, and A. Harrag, "Type-2 fuzzy logic controller based maximum power point tracking for photovoltaic systems," *Electr. Eng. & Electromech., no. 1, pp. 16–22, Jan. 2025.*

[5] A. A. Suryawanshi and A. Tapde, "Maximizing solar power output with PV STATCOM for reactive power compensation in on-grid systems," *Int. J. Intell. Syst. Appl. Eng., vol. 12, no. 21 Suppl., pp. 3382–3389, Mar. 2024.*

[6] G. Satpathy and D. De, "PV MPPT based one-cycle control of LV DC-fed three-leg single-phase STATCOM for high-quality grid current," *Electrical Engineering, vol. 106, pp. 4371–4386, Aug. 2024.*

[7] S. M. Al Hajri, F. J. Rodriguez, M. Liserre, and A. G. Al Haddad, "Advanced grid-filter design for MW-scale medium-voltage inverters: A frequency-domain optimization approach," *IEEE Trans. Ind. Electron., vol. 72, no. 2, pp. 1483–1494, Feb. 2025.*

[8] V. K. Govil, S. M. Tripathi, and K. Sahay, "Real-time assessment of PV-DSTATCOM for grid power quality enhancement using indirect current control strategy," *Scientific Reports, vol. 15, no. 19516, 2025.*

[9] T. A. Boghdady and Y. A. Mohamed, "Reactive power compensation using STATCOM in a PV grid-connected system with a modified MPPT method," *Ain Shams Eng. J., vol. 14, no. 8, 2023.*

[10] M. A. Mosleh and N. Umurkan, "Techno-economic control of UPFC against cyber-physical attacks considering power-system inter-area oscillations," *Appl. Sci., vol. 14, no. 12, Art. 5254, Jun. 2024.*

[11] F. G. Chremb and H. Medhaffar, "Power quality enhancement in transmission systems using STATCOM with type-1 and type-2 fuzzy logic controllers," *Int. J. Comput. Intell. Syst., vol. 17, no. 238, 2024.*

[12] S. A. Souri, A. Mehrizi-Sani, and K. Tehrani, "Stability enhancement of LCL-type grid-following inverters using capacitor voltage active damping," *IEEE Trans. Power Electron. (à vérifier publication finale).*

[13] L. Boukarana, "Control of a 400 kV power line by a STATCOM based on multilevel inverters using fuzzy regulators (FLC)," *Int. J. Appl. Eng. & Technol., vol. 6, no. 1, Jan. 2024.*

[14] J. Mao et al., "An adaptive MPPT algorithm for photovoltaic systems under partial shading conditions," *Sustain. Energy Technol. Assess., vol. 58, 2024.*

[15] F. P. Andrinirina et al, "Hybrid fuzzy logic and particle swarm optimization for MPPT under shading conditions," *arXiv preprint*, 2025.

[16] A. W. dos Santos Serra, L. A. S. Ribeiro, and M. Savaghebi, "Improved control for grid-following inverter with active damping and capacitor voltage decoupling," *IEEE ECCE*, 2025.

[17] N. G. El Sayed et al, "Artificial intelligent fuzzy control for LVRT improvement in PV/wind systems," *Scientific Reports*, vol. 14, 2024.

[18] J. Singh, S. P. Singh, and K. S. Verma, "Performance evaluation of LMPO-based MPPT technique for grid-integrated PV systems with LCL filter," *Processes, vol. 13, no. 3, 2025.*

[19] N. Singh and D. P. Kothari, "Enhanced reactive power control in PV inverters using sliding mode and fuzzy logic methods," *Energy Reports, vol. 10, pp. 893–905, 2024.*

[20] A. K. Khaliq et al, "Dynamic performance evaluation of STATCOM for renewable energy integration," *Int. Trans. Electr. Energy Syst.*, 2024.

[21] N. F. Ravelo et al.,
"Hybrid fuzzy logic control and shading-aware optimization for PV systems," *Renewable Energy / arXiv, 2025.*

[22] U. D. Annigeri and B. Singh, "Real-time implementation of MPPT and STATCOM for distributed PV systems," *IET Renew. Power Gen., vol. 17, no. 3, 2024.*

[23] M. I. Khan et al, "Fuzzy adaptive control of grid-interactive PV systems for power quality improvement," *IEEE Access, vol. 12, pp. 76543–76554, 2024.*

[24] A. Khaliq, H. Zahloul, and S. Salous, "Optimized design of LCL filter for grid-tied PV inverters under variable weather conditions," *IEEE Access*, 2025.

[25] L. Zhao et al, "Multi-objective optimization of PV-STATCOM controller parameters," *Control Engineering Practice, vol. 141, 2025.*

[26] Y. V. P. K. Rao and D. J. Pradeep, "Fuzzy-based current-controlled inverter for power quality improvement in PV systems," *Sustainability, vol. 17, no. 10, 2025.*

[27] Q. Hu and Z. Wei, "Design and analysis of LCL filter for medium-voltage PV inverters," *Energies, vol. 17, no. 8, 2024.*
[28] Z. Yin et al, "PLPR-based predictive control for LCL-filtered voltage source inverters," *IEEE Trans. Power Electronics, vol. 39, no. 6, 2024.*